VNU Journal of Science: Comp. Science & Com. Eng., Vol. 41, No. 1 (2025) 84–96

VNU Journal of Science:
Computer Science and Communication Engineering

Journal homepage: http://www.jcsce.vnu.edu.vn/index.php/jcsce

Original Article

A Versatile Beam Synthesis Algorithm for Reflection Beam Formation of RIS-aided Wireless Networks

Nguyen Thi Toan[1,3], Truong Vu Bang Giang[2], Nguyen Minh Tran[3*]

[1] *Hai Duong University, Hai Duong, Vietnam*
[2] *Vietnam National University (VNU), Hanoi, Vietnam*
[3] *VNU University of Engineering and Technology, Hanoi, Vietnam*

Received 24th March 2025
Revised 29th April 2025; Accepted 10th June 2025

Abstract: Reconfigurable intelligent surfaces are emerging as a cost-effective and power-efficient solution for future wireless networks. In this paper, a gradient descent-based beam synthesis (GD-based BS) algorithm is introduced for versatile reflection beam formation in RIS-aided wireless networks. The proposed solution optimizes the reflection coefficient vector of the RIS to form one beam or multiple beams with arbitrary beamwidth and nulling points. To accomplish this task, an objective function and its gradient are derived. Then, the proposed algorithm obtains the optimal solution by iteratively updating the reflection coefficient vector using the gradient. Simulation results demonstrate that the GD-based BS algorithm effectively synthesizes arbitrary reflection beams in the tested scenarios.

Keywords: RIS, beam synthesis, beam formation, gradient descent.

1. Introduction

In recent years, reconfigurable intelligent surfaces (RIS) have emerged as a revolutionary technology to enhance wireless communications by intelligently controlling the propagation environment [1, 2]. Unlike conventional active beamforming technology (i.e., phased array antenna), RIS passively reflects incident signals toward desired directions by dynamically adjusting their reflection phase shifts. Thus, RIS enables beamforming and beam synthesis without costly and power-hungry components (e.g., RF amplifiers, and RF phase shifters). This feature allows RIS to be massively and ubiquitously deployed in wireless networks. Moreover, with the capability of passive beamforming, RIS helps to improve spectral efficiency, and enhance signal coverage. Thus, these attractive features make RIS a promising solution for future wireless networks (i.e., B5G or 6G) [3].

*Corresponding author.
E-mail address: minhtran.nguyen@vnu.edu.vn

https://doi.org/10.25073/2588-1086/vnucsce.4728

Beam synthesis is a technique that optimizes the excitation signals of each element in a radiating array (e.g., an antenna array) to form a desired beam shape. Thus, this technique enhances wireless transmission efficiency over a wider coverage area through wide or multiple beams or reduces interference by forming null points. Several beam synthesis works have been extensively done for conventional phased array antennas with different configurations [4–16]. The beam synthesis problem has been resolved long ago with different approaches such as an iterative sampling method in [4], a two-step least squares (LS) method in [5], and convex optimization in [6]. Recently, several phase-only-based approaches have been proposed for linear, planar, and circular arrays [8–10]. In [11], a new approach based on zeros perturbation of the radiation pattern has been developed for both linear and planar arrays. [12] introduced a novel clustering method for synthesizing asymmetrically shaped beam patterns in linear antenna arrays. Authors in [13] presented a method that leverages the pattern diversity of dielectric resonator antenna (DRA) to synthesize the shaped beam pattern of passive antenna arrays. Different from the other works, [14] considered the array position certainty in the beam synthesis problem and proposed a robust pencil beam synthesis procedure. Besides, a mapping based optimization in [15] and a convex optimization in [16] have also been studied.

Similar to antenna arrays, RIS is also an array of massive passive elements that allows us to modify the characteristics of the incoming wave. Thus, synthesizing a reflection beam is also available and necessary for future RIS-assited wireless networks. However, unlike conventional beam synthesis techniques for active antenna arrays, the ones for RIS must confront the practical issue of phase limitation in RIS systems. Some recent works have been carried out for RIS beam synthesis [17–21]. Particularly, [18] and [20] proposed two different approaches to synthesize RIS beam patterns. Nevertheless, only continuous phase shift is considered, which is impractical in RIS. Considering discrete phase constraints in RIS, [17] introduced a minimization-maximization (MM) method to resolve the non-convex issues. However, this work did not comprehensively analyze the discrete phase shift effect on beam synthesis ability. Another technique has been studied for transmissive RIS in [19].

Unlike previous works, our approach exploits the passive nature of RIS while maintaining high flexibility in beam pattern synthesis. Existing approaches often focus on single-beam formation with idealized continuous-phase models, whereas our study provides a more comprehensive evaluation of practical phase quantization effects and multi-beam generation strategies. Through extensive numerical simulations, the effectiveness of the proposed algorithm in various RIS configurations and its ability to adapt to different communication scenarios will be demonstrated.

This paper presents a versatile beam synthesis algorithm for reflection beam formation in RIS-aided wireless networks. The proposed algorithm can generate various beam patterns, including a narrow wide beam (e.g., fan beams), a large square beam with a broad null, and multiple narrow beams (e.g., 2-3 beams), to address different wireless transmission requirements. Furthermore, the impact of varying quantization phase shift numbers on RIS beam synthesis performance, providing insights into the scalability and effectiveness of RIS configurations will be investigated.

The remainder of this paper is organized as follows: Section II presents the system model, including the overall geometric model and RIS's reflection characteristics. Section III details the synthesis of the RIS reflection pattern based on the gradient descent algorithm. Section IV provides simulation results and verification. Finally, Section V concludes the paper and discusses future research directions.

2. System Model

2.1. Overall Geometry Model

An RIS-aided wireless communication system in which the RIS helps to reflect and form the beams to the desired end users as depicted in Fig. 1 is being considered. Generally speaking, the system contains one rectangular RIS that reflects the transmitted signal from one transmitter to the desired receivers. The RIS is a M-by-N uniform planar array in which M and N are, respectively, the number of unit cells in the x and y directions. The total number of unit cells in the RIS is denoted by $N^{\text{RIS}} = M \times N$. Let d_x and d_y denote the element spacing along the x-axis and y-axis, respectively. Each unit cell in the RIS is indexed by $n = 1, \ldots, N^{\text{RIS}}$ in the column-major order. The transmitter (Tx) is equipped with one high-gain antenna (e.g., a horn), which is located at $s^{\text{Tx}} = (r^{\text{Tx}}, \theta^{\text{Tx}}, \phi^{\text{Tx}})^T$ in the global coordinate in which the center of RIS is positioned at the origin. The transmitter and the RIS can communicate through a wireless or physical link. Therefore, the transmitter can direct its main beam towards the RIS.

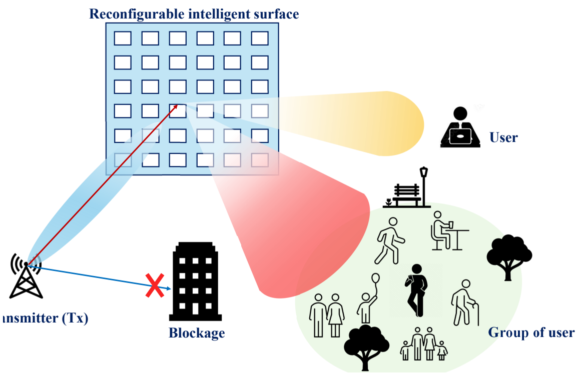

Figure 1. Reflection beam formation in RIS-aided wireless network.

2.2. RIS Reflection Characterization

The Tx antenna radiates electromagnetic waves (EM waves) that carry communication data toward the RIS. These EM waves are then reflected at the RIS before being delivered to the desired receivers. Under the far-field assumption, the incident electric field (E-field) vector at the unit cell n can be expressed as

$$\mathbf{E}_n^{\text{inc}} = \frac{\mathbf{E}^{\text{Tx}}(\theta^{\text{Tx}}, \phi^{\text{Tx}})}{r^{\text{Tx}}} \exp(-j\kappa r_n), \qquad (1)$$

where $\mathbf{E}^{\text{Tx}}(\theta^{\text{Tx}}, \phi^{\text{Tx}}) = E_\theta^{\text{Tx}}(\theta^{\text{Tx}}, \phi^{\text{Tx}})\mathbf{a}_\theta + E_\phi^{\text{Tx}}(\theta^{\text{Tx}}, \phi^{\text{Tx}})\mathbf{a}_\phi$ is the E-field vector of the Tx in the direction $(\theta^{\text{Tx}}, \phi^{\text{Tx}})$, $\mathbf{a}_\theta$ and $\mathbf{a}_\phi$ are, respectively, the unit vectors in the zenith and azimuth directions, j is the imaginary unit, $\kappa = 2\pi/\lambda$ is the wave number, λ is the wavelength at the operating frequency, r_n is the distance between the Tx and the unit cell n in the RIS. The unit cell n converts the incident EM waves into guided waves and then manipulates them by controlling its reflection coefficient before re-radiating to the free space. In practice, the RIS is designed with discrete reflection phases to reduce implementation costs and complexity. Let us consider a RIS with ξ-bit phase shift that equals $\chi = 2^\xi$ available discrete phase shifts. Without loss of generality, the reflection coefficient of the unit cell n can be described as

$$\Gamma_n = \Lambda_\chi\left(\exp\left(j\varphi_n\right)\right), \qquad (2)$$

where φ_n is the continuous reflection phase of the unit cell n, $\Lambda_\chi(\cdot)$ is the phase quantization function. For a complex number z, the phase quantization is defined as follows

$$\Lambda_\chi(z) = |z| \exp\left(j\frac{2\pi}{\chi}\left\lfloor\frac{\chi}{2\pi}\angle z + 0.5\right\rfloor\right), \qquad (3)$$

where $|z|$ and $\angle z$ are the magnitude and phase of z. Note that the reflection magnitude is normalized to 1 since most of practical RIS works only need to manipulate their reflection phase for beamforming. Then, the total reflecting E-field from the RIS can be written as

$$\mathbf{E}^{\mathrm{re}}(\theta,\phi;\mathbf{g}) = \Upsilon_0 \sum_{n=1}^{N^{\mathrm{RIS}}} \Gamma_n \exp(j\kappa \mathbf{p}_n^T \mathbf{u}(\theta,\phi))\mathbf{E}_n^{\mathrm{inc}} \tag{4}$$

$$= \mathbf{f}^T(\theta,\phi)\mathbf{g}, \tag{5}$$

where $\mathbf{u}(\theta,\phi) = (\sin\theta\cos\phi, \sin\theta\sin\phi, \cos\theta)^T$ is the spherical unit vector, $\mathbf{p}_n = (p_n^x, p_n^y, p_n^z)^T$ denotes the position vector of the unit cell n in the global coordinate, $\Upsilon_0 = |E_0(\theta,\phi)|e^{j\kappa r}/r$ is the radiated E-field intensity of a single unit cell at a point of interest, $\mathbf{g}$ is the reflection coefficient vector of the RIS which is defined as

$$\mathbf{g} = (\Gamma_1, \Gamma_2, \ldots, \Gamma_{N^{RIS}})^T, \tag{6}$$

and $\mathbf{f}(\theta,\phi)$ is array response vector that is

$$\mathbf{f}(\theta,\phi) = (f_1(\theta,\phi), f_2(\theta,\phi), \ldots, f_{N^{RIS}}(\theta,\phi))^T, \tag{7}$$

and

$$f_n(\theta,\phi) = \Upsilon_0 \exp(j\kappa(p_n^x \sin\theta\cos\phi + p_n^y \sin\theta\sin\phi + p_n^z\cos\theta))\mathbf{E}_n^{\mathrm{inc}}. \tag{8}$$

The directivity of the reflected beam pattern from the RIS can be defined as one for an antenna. The directivity toward the direction of (θ,ϕ) in the far-field zone can be defined as

$$D(\theta,\phi;\mathbf{g}) = \frac{4\pi U(\theta,\phi;\mathbf{g})}{P_{\mathrm{rad}}(\mathbf{g})} \tag{9}$$

where $U(\theta,\phi;\mathbf{g})$ is the radiation intensity of the RIS toward direction (θ,ϕ) in the far-field zone that is

$$U(\theta,\phi;\mathbf{g}) \approx \frac{1}{2\eta}|\mathbf{E}^{\mathrm{re}}(\theta,\phi;\mathbf{g})|^2, \tag{10}$$

$P_{\mathrm{rad}}(\mathbf{g})$ is the total reflection power with the reflection coefficient vector $\mathbf{g}$ at the RIS that is computed by integrating the radiation intensity over the entire direction. The total reflection power can be written as

$$P_{\mathrm{rad}}(\mathbf{g}) = \int_{(\theta,\phi)\in\mathcal{S}} U(\theta,\phi;\mathbf{g})\sin\theta d\theta d\phi, \tag{11}$$

where $\mathcal{S} = \{(\theta,\phi)|\ 0 \le \theta \le \pi,\ 0 \le \phi \le 2\pi\}$ is the all direction angles. From (5), (9), (10), and (11), the directivity of the reflected beam from the RIS can be rewritten as

$$D(\theta,\phi;\mathbf{g}) = \frac{4\pi|\mathbf{E}^{\mathrm{re}}(\theta,\phi;\mathbf{g})|^2}{\int_{\theta,\phi)\in\mathcal{S}} |\mathbf{E}^{\mathrm{re}}(\theta,\phi;\mathbf{g})|^2 \sin\theta d\theta d\phi} = \frac{\mathbf{g}^H\mathbf{F}(\theta,\phi)\mathbf{g}}{\mathbf{g}^H\mathbf{\Sigma}\mathbf{g}}, \tag{12}$$

where

$$\mathbf{F}(\theta,\phi) = \mathbf{f}^*(\theta,\phi)\mathbf{f}^T(\theta,\phi), \tag{13}$$

and

$$\mathbf{\Sigma} = \frac{1}{4\pi}\int_{(\theta,\phi)\in\mathcal{S}} \mathbf{f}^*(\theta,\phi)\mathbf{f}^T(\theta,\phi)\sin\theta d\theta d\phi. \tag{14}$$

It can be deduced from (12) that the directivity of the reflected beam of the RIS mainly depends on the array configuration (i.e., $\mathbf{f}(\theta,\phi)$) and the reflection coefficient vector of the RIS (i.e., $\mathbf{g}$). Intuitively, one can optimize the array geometry or the reflection response of each unit cell in the RIS to adjust the directivity in a particular direction (θ,ϕ). However, in this work, only the reflection coefficient vector of the RIS is optimized to achieve our target.

3. Gradient Descent Based RIS Reflection Pattern Synthesis

In this section, the objective function will be developed and the gradient descent method will be applied to seek the optimal solution. The proposed algorithm optimizes the reflection coefficient vector for the RIS to form one or multiple beams toward desired directions and form null points to undesired directions.

3.1. Objective Function Development

In this subsection, firstly, the objective function will be defined to be maximized to achieve the target. Indeed, our target is to form beams toward desired directions (i.e., users) and direct the null points toward undesired directions. While the beam is an angular region with the highest directivity compared to the other regions surrounding it, a null point has the lowest directivity.

Let us first derive the average directivity over an angular region. The angular region is a vector of zenith and azimuth (i.e., (θ, ϕ)). Thus, the average directivity of the RIS with the reflection coefficient vector $\mathbf{g}$ over a given angular region Ω can be computed as

$$\mathcal{A}(\Omega; \mathbf{g}) = \frac{\int_{(\theta,\phi)\in\Omega} D(\theta, \phi; \mathbf{g}) \sin\theta d\theta d\phi}{\int_{(\theta,\phi)\in\Omega} \sin\theta d\theta d\phi} \tag{15}$$

$$= \frac{\mathbf{g}^H \mathbf{\Xi}(\Omega)\mathbf{g}}{\mathbf{g}^H \mathbf{\Sigma}\mathbf{g}}, \tag{16}$$

where

$$\mathbf{\Xi}(\Omega) = \frac{1}{Q} \int_{(\theta,\phi)\in\Omega} \mathbf{F}(\theta, \phi) \sin\theta d\theta d\phi, \tag{17}$$

and $Q = \int_{(\theta,\phi)\in\Omega} \sin\theta d\theta d\phi$. Let Ω^b and Ω^n denote the angular regions of a beam and a null point, respectively. Then, our target is to maximizing $\mathcal{A}(\Omega^b; \mathbf{g})$ while minimizing $\mathcal{A}(\Omega^n; \mathbf{g})$. The simple objective function can be defined as

$$\mathcal{J}_0(\mathbf{g}) = \mathcal{A}(\Omega^b; \mathbf{g}) - \mathcal{A}(\Omega^n; \mathbf{g}). \tag{18}$$

Nevertheless, the directivity might be only maximized or minimized at some points in the angular region Ω^b or Ω^n. To ensure the flatness of the directivity over the target region, minimization of the variance of the directivity in the objective function will be considered. The variance of the directivity $\mathcal{V}(\Omega; \mathbf{g})$ over the angular region Ω can be calculated as

$$\mathcal{V}(\Omega; \mathbf{g}) = \frac{1}{Q} \int_{(\theta,\phi)\in\Omega} (D(\theta, \phi; \mathbf{g}) - \mathcal{A}(\Omega; \mathbf{g}))^2 \sin\theta d\theta d\phi. \tag{19}$$

Hence, the objective function is now defined as

$$\begin{aligned} \mathcal{J}(\mathbf{g}) = &\mathcal{A}(\Omega^b; \mathbf{g}) - \mathcal{A}(\Omega^n; \mathbf{g}) \\ &- \sigma(\mathcal{V}(\Omega^b; \mathbf{g}) + \mathcal{V}(\Omega^n; \mathbf{g})), \end{aligned} \tag{20}$$

where σ is the flatness control parameter. In addition, for facilitating the problem, the Kronecker product ($\otimes$) is utilized to simplify the objective function. Indeed, the variance $\mathcal{V}(\Omega; \mathbf{g})$ can be rewritten as

$$\mathcal{V}(\Omega; \mathbf{g}) = \frac{\mathbf{G}^H \mathbf{\Psi}(\Omega)\mathbf{G}}{\mathbf{G}^H \mathbf{\Phi}\mathbf{G}}, \tag{21}$$

where

$$\mathbf{G} = \mathbf{g} \otimes \mathbf{g}, \tag{22}$$

$$\mathbf{\Phi} = \mathbf{\Sigma} \otimes \mathbf{\Sigma}, \tag{23}$$

and

$$\begin{aligned} \mathbf{\Psi}(\Omega) = &\frac{1}{Q} \int_{(\theta,\phi)\in\Omega} \mathbf{F}(\theta, \phi) \otimes \mathbf{F}(\theta, \phi) \sin\theta d\theta d\phi \\ &- \mathbf{\Xi}(\Omega) \otimes \mathbf{\Xi}(\Omega). \end{aligned} \tag{24}$$

Thus, from (20), (16), and (21), the objective function can be rewritten as

$$\begin{aligned} \mathcal{J}(\mathbf{g}) &= \frac{\mathbf{g}^H \mathbf{\Xi}(\Omega^b)\mathbf{g}}{\mathbf{g}^H \mathbf{\Sigma}\mathbf{g}} - \frac{\mathbf{g}^H \mathbf{\Xi}(\Omega^n)\mathbf{g}}{\mathbf{g}^H \mathbf{\Sigma}\mathbf{g}} \\ &\quad - \sigma\left(\frac{\mathbf{G}^H \mathbf{\Psi}(\Omega^b)\mathbf{G}}{\mathbf{G}^H \mathbf{\Phi}\mathbf{G}} + \frac{\mathbf{G}^H \mathbf{\Psi}(\Omega^n)\mathbf{G}}{\mathbf{G}^H \mathbf{\Phi}\mathbf{G}}\right) \\ &= \frac{\mathbf{g}^H \mathbf{\Xi}\mathbf{g}}{\mathbf{g}^H \mathbf{\Sigma}\mathbf{g}} - \sigma\frac{\mathbf{G}^H \mathbf{\Psi}\mathbf{G}}{\mathbf{G}^H \mathbf{\Phi}\mathbf{G}}, \end{aligned} \tag{25}$$

where

$$\mathbf{\Xi} = \mathbf{\Xi}(\Omega^b) - \mathbf{\Xi}(\Omega^n), \tag{26}$$

and

$$\mathbf{\Psi} = \mathbf{\Psi}(\Omega^b) + \mathbf{\Psi}(\Omega^n). \tag{27}$$

It can be realized that the objective function in (20) is a convex function. Therefore, any optimization method for convex problems can be used for finding the optimal solution. In the next subsection, the gradient descent algorithm to maximize the objective function which is aligned with our target will be demonstrated.

3.2. Gradient Descent Algorithm

Gradient descent (GD) is a first-order iterative algorithm for optimizing differentiable multivariate functions. The GD approach iteratively updates the variable that moves toward the objective function's maximum or minimum by using its gradient at the current point. For example, let us consider a differentiable function $f(\mathbf{x})$ with the gradient $\nabla_{\mathbf{x}} f$. Then, $f(\mathbf{x})$ decreases fastest if one goes from $\mathbf{x}_i$ in the direction of the negative gradient of f at $\mathbf{x}_i$, $\nabla_{\mathbf{x}_i} f$. Thus, the next point that minimizes $f(\mathbf{x})$ can be updated as

$$\mathbf{x}_{i+1} = \mathbf{x}_i - \eta \nabla_{\mathbf{x}_i} f, \quad (28)$$

where $\eta \in \mathbb{R}^+$ is the learning rate. Note that the subtraction in (28) should change to addition for a maximizing problem. Hence, the maximum or minimum of $f(\mathbf{x})$ can be obtained by iteratively updating the new position of $\mathbf{x}$.

To apply the GD algorithm, the gradient of the objective function in (20) is firstly obtained for the optimization variable (i.e., $\mathbf{g}$). Moreover, the reflection coefficient vector is a complex vector with unchanged magnitudes and varied phases. Thus, the gradient of $\mathcal{J}(\mathbf{g})$ is only calculated with respect to the phase variable in $\mathbf{g}$ such that

$$\nabla_{\mathbf{g}} \mathcal{J} = \nabla_{\boldsymbol{\varphi}} \mathcal{J} = \left(\frac{\partial \mathcal{J}}{\partial \varphi_1}, \frac{\partial \mathcal{J}}{\partial \varphi_2}, \ldots, \frac{\partial \mathcal{J}}{\partial \varphi_{N^{RIS}}} \right)^T, \quad (29)$$

where $\boldsymbol{\varphi} = (\varphi_1, \varphi_2, \ldots, \varphi_{N^{\mathrm{RIS}}})^T$, φ_n is the phase of Γ_n. Applying the chain rule, the gradient in (29) can be computed as

$$\frac{\partial \mathcal{J}}{\partial \varphi_n} = \frac{\partial \Gamma_n}{\partial \varphi_n} \frac{\partial \mathcal{J}}{\partial \Gamma_n} + \frac{\partial \Gamma_n^*}{\partial \varphi_n} \frac{\partial \mathcal{J}}{\partial \Gamma_n^*}, \quad (30)$$

where $\Gamma_n^* = \Lambda_\chi(\exp(-j\varphi_n))$ is the complex conjugate of Γ_n. Thus, to calculate the gradient of the complex function $\mathcal{J}(\mathbf{g})$, an additional variable $\mathbf{h} = (h_1, h_2, \ldots, h_{N^{\mathrm{RIS}}})$ with $h_n = \Gamma_n^* = \Lambda_\chi(\exp(-j\varphi_n))$ is introduced. The objective function can now be expressed as

$$\mathcal{J}(\mathbf{g}, \mathbf{h}) = \frac{\mathbf{h}^T \boldsymbol{\Xi} \mathbf{g}}{\mathbf{h}^T \boldsymbol{\Sigma} \mathbf{g}} - \sigma \frac{\mathbf{H}^T \boldsymbol{\Psi} \mathbf{G}}{\mathbf{H}^T \boldsymbol{\Phi} \mathbf{G}}, \quad (31)$$

where $\mathbf{H} = \mathbf{h} \otimes \mathbf{h}$. In (31), $\mathbf{g}$ and $\mathbf{h}$ are treated as two independent variables. Afterward, the gradient of $\mathcal{J}(\mathbf{g}, \mathbf{h})$ with respect to $\mathbf{g}$ and $\mathbf{h}$ can be obtained as follows [22]

$$\begin{aligned}\nabla_{\mathbf{g}} \mathcal{J} =& \frac{\boldsymbol{\Xi}^* \mathbf{h} (\mathbf{h}^T \boldsymbol{\Sigma} \mathbf{g}) - (\mathbf{h}^T \boldsymbol{\Sigma} \mathbf{g}) \boldsymbol{\Sigma}^* \mathbf{h}}{(\mathbf{h}^T \boldsymbol{\Sigma} \mathbf{g})^2} \\ & - \sigma \frac{\mathbf{G}' \boldsymbol{\Psi}^* \mathbf{H} (\mathbf{H}^T \boldsymbol{\Phi} \mathbf{G}) - (\mathbf{H}^T \boldsymbol{\Phi} \mathbf{G}) \mathbf{G}' \boldsymbol{\Phi}^* \mathbf{H}}{(\mathbf{H}^T \boldsymbol{\Phi} \mathbf{G})^2},\end{aligned} \quad (32)$$

where $\mathbf{G}' = \mathbf{I}_N \otimes \mathbf{g}^T + \mathbf{g}^T \otimes \mathbf{I}_N$, and $\mathbf{I}_N$ is the $N \times N$ identity matrix.

$$\begin{aligned}\nabla_{\mathbf{h}} \mathcal{J} =& \frac{\boldsymbol{\Xi} \mathbf{g} (\mathbf{h}^T \boldsymbol{\Sigma} \mathbf{g}) - (\mathbf{h}^T \boldsymbol{\Sigma} \mathbf{g}) \boldsymbol{\Sigma} \mathbf{g}}{(\mathbf{h}^T \boldsymbol{\Sigma} \mathbf{g})^2} \\ & - \sigma \frac{\mathbf{H}' \boldsymbol{\Psi} \mathbf{G} (\mathbf{H}^T \boldsymbol{\Phi} \mathbf{G}) - (\mathbf{H}^T \boldsymbol{\Phi} \mathbf{G}) \mathbf{H}' \boldsymbol{\Phi} \mathbf{G}}{(\mathbf{H}^T \boldsymbol{\Phi} \mathbf{G})^2},\end{aligned} \quad (33)$$

where $\mathbf{H}' = \mathbf{I}_N \otimes \mathbf{h}^T + \mathbf{h}^T \otimes \mathbf{I}_N$. Furthermore, in (30) we can also obtain

$$\frac{\partial \Gamma_n}{\partial \varphi_n} = j \Lambda_\chi(\exp(j\varphi_n)) = j\Gamma_n \quad (34)$$

$$\frac{\partial \Gamma_n^*}{\partial \varphi_n} = -j \Lambda_\chi(\exp(j\varphi_n)) = -j\Gamma_n^*. \quad (35)$$

Thus, from (29), (30), (32), (33), (34), and (35), $\nabla_{\boldsymbol{\varphi}} \mathcal{J}$ can be derived as follows

$$\nabla_{\boldsymbol{\varphi}} \mathcal{J} = j\mathbf{g} \odot \nabla_{\mathbf{g}} \mathcal{J} - j\mathbf{h} \odot \nabla_{\mathbf{h}} \mathcal{J}, \quad (36)$$

where $\odot$ is the Hadamard product.

Since our aim is to maximize the objective function $\mathcal{J}(\mathbf{g})$, the variable $\mathbf{g}$ can be updated as

$$\boldsymbol{\varphi}_{i+1} = \boldsymbol{\varphi}_i + \eta \nabla_{\boldsymbol{\varphi}_i} \mathcal{J} \quad (37)$$

$$\mathbf{g}_{i+1} = \Lambda_\chi(\exp(j\boldsymbol{\varphi}_{i+1})), \quad (38)$$

where $\boldsymbol{\varphi}_i$ and $\mathbf{g}_i$ are, respectively, the reflection phase vector and reflection coefficient vectors in ith iteration. Consequently, the gradient descent-based beam synthesis algorithm (GD-based BS algorithm) is obtained and interpreted in Algorithm 1.

Algorithm 1: GD-based BS Algorithm

Input:
Number of unit cells N^{RIS}
Transmitter position s^{Tx}
Angular region of desired beam Ω^b
Angular region of null point Ω^n
Number of available phase shift χ
Learning rate η, and iteration number K
Output:
Optimal reflection coefficient vector $\mathbf{g}^{\mathrm{opt}}$
Best cost value $\mathcal{J}^{\mathrm{best}}$

Construct the objective function $\mathcal{J}(\mathbf{g}, \mathbf{h})$
Initialize $\boldsymbol{\varphi}_0 \leftarrow \mathrm{rand}(\chi, N^{\mathrm{RIS}})2\pi/\chi$
$\mathbf{g}_0 \leftarrow \Lambda_\chi(\exp(j\boldsymbol{\varphi}_0))$
$k \leftarrow 0$, and $\mathcal{J}^{\mathrm{best}} \leftarrow 0$
while $k < K$ **do**
  Compute the gradient $\nabla_{\mathbf{g}_k}\mathcal{J}$ and $\nabla_{\mathbf{h}_k}\mathcal{J}$
  Calculate the gradient $\nabla_{\boldsymbol{\varphi}_k}\mathcal{J}$
  $\boldsymbol{\varphi}_{k+1} = \boldsymbol{\varphi}_k + \eta\nabla_{\boldsymbol{\varphi}_k}\mathcal{J}$
  $\mathbf{g}_{k+1} = \Lambda_\chi(\exp(j\boldsymbol{\varphi}_{k+1}))$
  Compute $\mathcal{J}(\mathbf{g}_{k+1})$
  if $\mathcal{J}(\mathbf{g}_{k+1}) > \mathcal{J}^{best}$ **then**
    $\mathcal{J}^{\mathrm{best}} \leftarrow \mathcal{J}(\mathbf{g}_{k+1})$
    $\mathbf{g}^{\mathrm{tmp}} = \mathbf{g}_{k+1}$
  end
  $k = k + 1$
end
$\mathbf{g}^{\mathrm{opt}} \leftarrow \mathbf{g}^{\mathrm{tmp}}$
return $\mathbf{g}^{\mathrm{opt}}$ and $\mathcal{J}^{\mathrm{best}}$

4. Simulation and Verification

This section presents an evaluation of the proposed algorithm through various simulation scenarios. First, its effectiveness in generating the intended beam and accurately positioning the null point is being assessed. Next, the influence of the number of discrete phase shifts on the algorithm's performance will be examined. Lastly, the capability to form broad nulls and multiple beams is being demonstrated.

In the simulation, the RIS is a planar array with 12×12 unit cells and positioned at the origin of the global coordinate. The adjacent unit cell spacing in RIS is set to 0.55λ in both x and y directions (λ is the operating wavelength). The transmitter (Tx) is placed at (3 m, $30°, -45°$) in the global coordinate. The learning rate (η) is set to 0.35. In addition, the iteration number (K) is 100. The above setup is consistent throughout this section; the other configurations will be stated in the subsection.

4.1. Beam and Null Formation

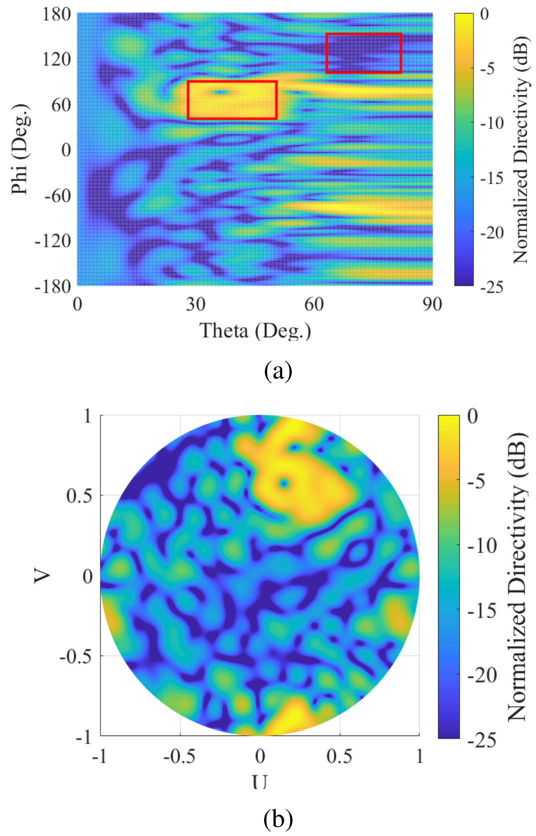

Figure 2. Normalized directivity: (a) (θ, ϕ) plane, (b) u-v plane.

To evaluate the ability of beam and null formation, the angular region for a beam at $\Omega^b = [(\theta^b, \phi^b)|\ 30° \le \theta^b \le 50°,\ 45° \le \phi^b \le 90°]$ and a null at $\Omega^n = [(\theta^n, \phi^n)|\ 60° \le \theta^b \le 80°,\ 100° \le \phi^b \le 150°]$ is being set. A 3-bit RIS or 8 available phase shifts in the RIS is being considered.

Fig. 2 shows the simulation results of the normalized directivity in (θ, ϕ) plane (i.e., Fig. 2(a)) and u-v plane (i.e., Fig. 2(b)) for this scenario. It is clear that the proposed algorithm can effectively yield a wide rectangular-shaped beam and a broad null at the desired angular regions. The gap of the directivity between the main beam and the null is around 25 dB. In other words, the transmission for desired users is ensured in the main beam region while the interference to the undesired users is suppressed at the null region.

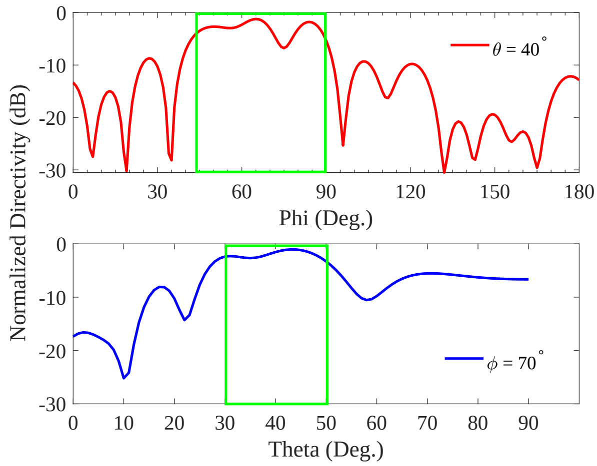

Figure 3. Beam pattern with respect to θ and ϕ at the beam region.

Fig. 3 and Fig. 4 detail the beam pattern with respect to zenith and azimuth directions at the beam and null, respectively. These results are sampled at the middle of the beam and null angular regions. For example, the subfigure at the top of Fig. 3 is the beam pattern with respect to azimuth angle (i.e., ϕ (deg.)) and $\theta = (\theta_l^b + \theta_u^b)/2 = 40°$, where θ_l^b and θ_u^b are the lower and upper boundaries of θ^b, respectively. Fig. 3 demonstrates that a beam is well formed toward the azimuth direction between 40° and 90° and zenith angles from 30° to 50°, which meet well with the target angular region. On the other hand, a broad null is clearly established at the angular region of the target null as shown in

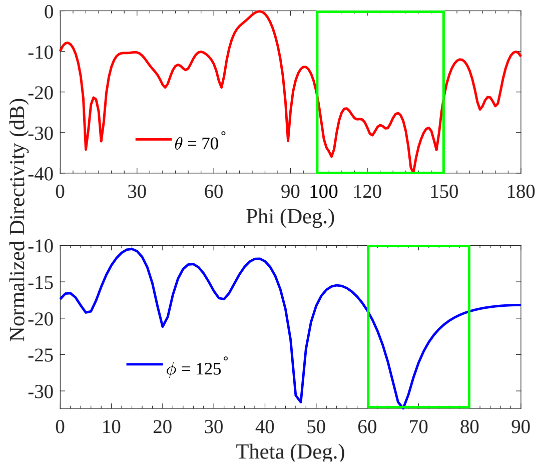

Figure 4. Beam pattern with respect to θ and ϕ at the null region.

Fig. 4. These results confirm the effectiveness of the proposed algorithm in forming a beam and a null simultaneously.

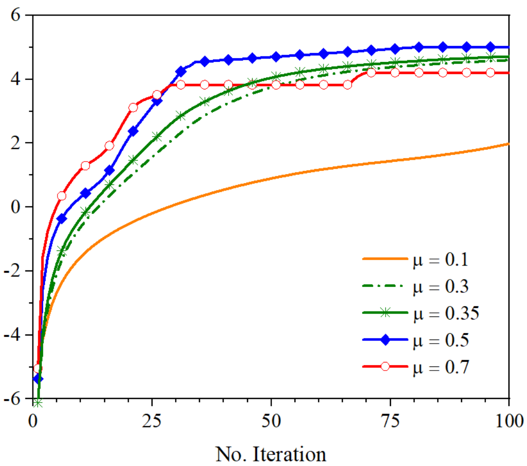

Figure 5. Convergence of the proposed method with different learning rate.

The convergence rate of the proposed method with different learning rates is shown in Fig. 5. In this simulation, we vary the learning rate from 0.1 to 0.7. As the learning is set to 0.1, the method slowly converges to the optimal point. The method converges quickly as the learning rate gets bigger. Nevertheless, the method oscillates over the optimal point when the learning rate is 0.7. Thus, the optimal learning rate value lies between 0.3 and 0.5. It shows that the cost value approaches a stable value after around 85 iterations with the learning rate ranging from 0.3 to 0.5. It means that the proposed method has converged.

The corresponding reflection phase of the RIS after accomplishing the algorithm is given in Fig. 6.

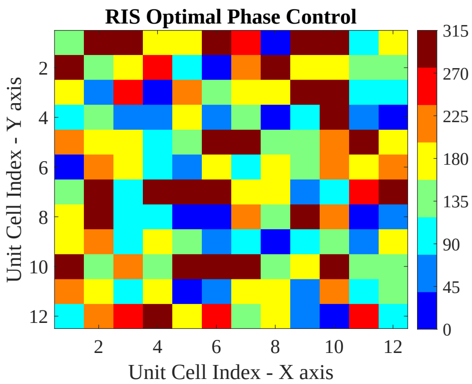

Figure 6. Optimal RIS reflection phase.

4.2. *Quantization Phase Effect*

This subsection analyses the impact of the RIS quantization phase shift on the proposed algorithm's performance. Four different phase shift numbers, 2, 4, 8, and 16, are considered in this simulation. In other words, these four different phase shifts correspond to "1-bit", "2-bit", "3-bit", and "4-bit" phase changes. For notation convenience, the latter is named after the corresponding results. Furthermore, this investigation only performs with one broad beam formation of the proposed algorithm. Indeed, the desired beam is set at $\Omega^b = [(\theta^b, \phi^b)|\ 30° \leq \theta^b \leq 40°,\ 40° \leq \phi^b \leq 120°]$.

The simulation beam patterns with different quantization phase shifts are depicted in Fig. 7. It can be observed that though the phase shift is limited to 1-bit, our algorithm can still synthesize a broad beam matched with a target angular region. Specifically, the "4-bit" case yields the best results with sharp and clear beam over the desired angular region. On the other hand, due to the limited phase shift, the beam pattern shape in 1-bit RIS flucates over the desired range (see Fig. 7(a)). In addition, the directivity of the "1-bit" case is lower than that of the higher phase shift resolution. It is obvious since the composite reflected EM waves at the beam region are constructively but not ideally added up with limited phase shift. However, a broad beam can be witnessed at the target angular region. The corresponding optimal reflection phase shifts of these four cases are given in Fig. 8.

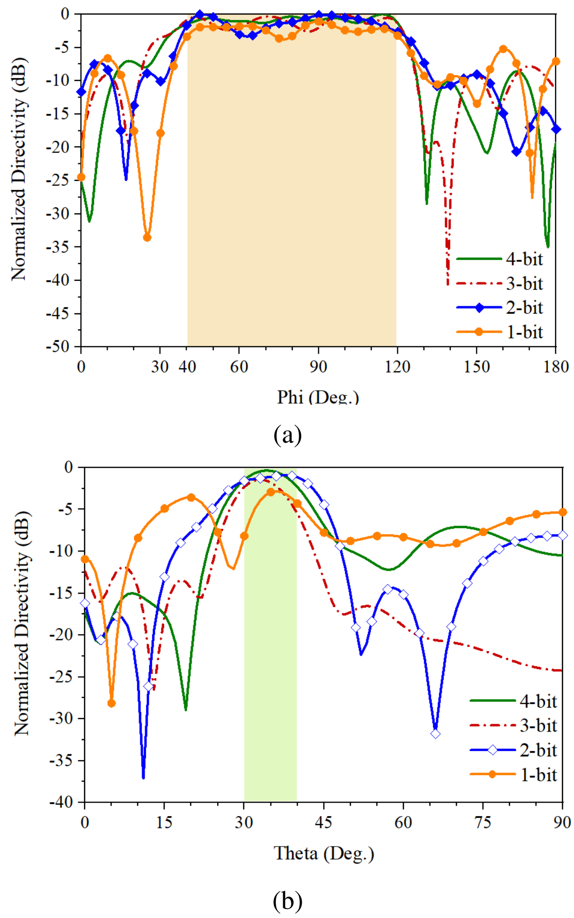

Figure 7. Beam pattern with respect to: (a) azimuth angle (ϕ); (b) zenith angle (θ) at the beam region.

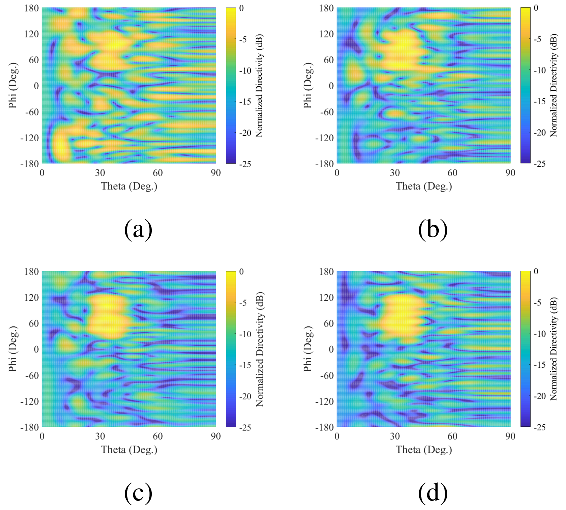

Figure 8. Normalized directivity over 2D zenith-azimuth angles: (a) 1-bit; (b) 2-bit; (c) 3-bit; (d) 4-bit.

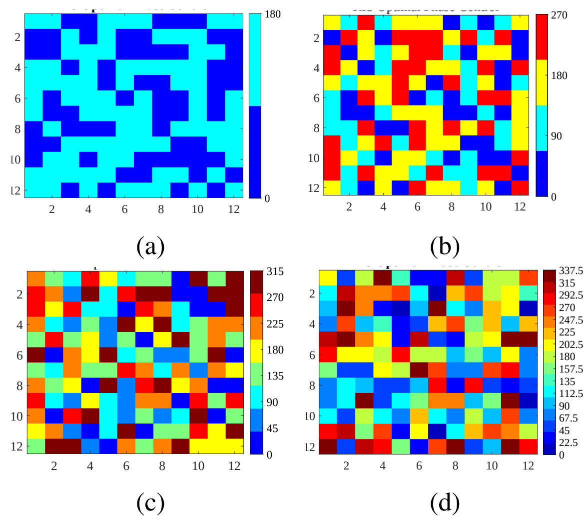

Figure 9. Optimal RIS reflection phase distribution: (a) 1-bit; (b) 2-bit; (c) 3-bit; (d) 4-bit.

The corresponding normalized directivity over zenith and azimuth directions of the four phase shifts is presented in Fig. 9. While distorted wide beams with high side lobes are formed for "1-bit" and "2-bit", well-shaped wide beams are formed for both "3-bit" and "4-bit" cases. The beams in the latter two cases are almost the same, showing the saturation of the phase shift number. In other words, increasing RIS phase shift resolution, which is beyond "3-bit" does not make much improvement in beamforming.

4.3. Multiple Reflection Beam

In this subsection, the capability of forming multiple reflection beams of the proposed solution is being tested. Particularly, three different beams are being formed at three different angular regions that are

$$\Omega_1^b = [(\theta_1^b, \phi_1^b)|\ 20^\circ \leq \theta_1^b \leq 30^\circ,\ 30^\circ \leq \phi_1^b \leq 50^\circ], \quad (39)$$

$$\Omega_2^b = [(\theta_2^b, \phi_2^b)|\ 40^\circ \leq \theta_2^b \leq 50^\circ,\ 60^\circ \leq \phi_2^b \leq 80^\circ], \quad (40)$$

$$\Omega_3^b = [(\theta_3^b, \phi_3^b)|\ 60^\circ \leq \theta_3^b \leq 70^\circ,\ 90^\circ \leq \phi_3^b \leq 110^\circ]. \quad (41)$$

The available phase shift number is set to 4 or equivalent to 2-bit. Fig. 10 indicates the simulation results of multiple beam scenario. As can be seen from Fig. 10(a), three beams is exactly synthesized at the target regions. There is one specular lobe formed around $-90^\circ \leq \phi^s \leq -110^\circ$ and $60^\circ \leq \theta^s \leq 90^\circ$. This is an issue of the quantization effect in RIS, which can be addressed by setting the objective function to eliminate the beam at the specular direction.

4.4. Complexity Analysis and Comparison

As we have investigated, gradient descent (GD) is one of the most popular optimization techniques for convex optimization problems due to its low complexity and rapid convergence rate. Indeed, the computation complexity of our algorithm is $O(NKP)$, where $N = N^{RIS}$ is the total number of unit cell, K is the number of iterations, P is the total grid points in the beam and null regions.

Table 1 shows the comparison between our proposed approach with the other existing works. It can be observed that our GD-based BS method has low complexity, versatile beam, and null formation ability. Moreover, our algorithm

Table 1. Comparison between our proposal and previous existing works

Approach	**Optimization Method**	**Complexity**	**Formation Ability**		**RIS Phase**	**RIS Configuration**
			Beam	**Null**		
[17]	MM	$O(N^3KP)$	wide	NA	1-bit	passive (UPA)
[18]	ADMM	$O(K(NP + N^2 + N^3))$	wide	narrow	continuous	active (ULA)
[19]	BIS	$O(NKP)$	wide, multiple	narrow	continuous	passive (ULA)
This work	GD	$O(NKP)$	wide, multiple	wide, multiple	quantized	passive (UPA)
Note:	K: number of iterations, N: number of unit cells in RIS, P: total number of grid points in the beam/null regions.					

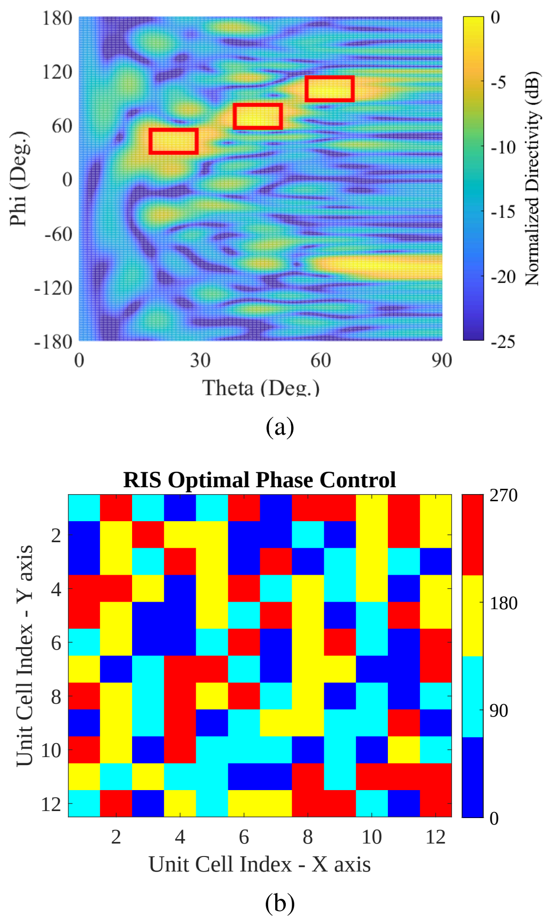

Figure 10. Multiple beam simulation results: (a) normalized directivity over zenith and azimuth directions; (b) RIS optimal reflection phase shift.

can effectively work with passive and quantized phase UPA-shaped RISs, which is more practical compared to [18] and [19].

5. Conclusion

In this paper, a gradient descent-based beam synthesis (GD-based BS) algorithm has been designed for multi-functional beamforming in RIS-aided wireless networks. A closed-form expression for the objective function and an iterative solution have been derived. Numerical simulations under various scenarios have been conducted to evaluate the performance of the algorithm. The results show that the proposed algorithm is capable of generating arbitrary beams and nulls that satisfy specified targets. In particular, it can optimize the RIS to create a rectangular-shaped beam with a null, a broad beam, and multiple beams. Moreover, the study has examined the influence of the number of available phase shifts on performance, demonstrating that the algorithm effectively forms the desired beam and null patterns even when the phase shift resolution is limited.

Acknowledgment

This work has been supported by VNU University of Engineering and Technology under project number CN24.09.

References

[1] M. Di Renzo et al., "Smart Radio Environments Empowered by Reconfigurable Intelligent Surfaces: How It Works, State of Research, and The Road Ahead," in *IEEE J. Sel. Areas Commun.*, vol. 38, no. 11, pp. 2450–2525, Nov. 2020.

[2] W. Tang et al., "Wireless Communications With Reconfigurable Intelligent Surface: Path Loss Modeling and Experimental Measurement," in *IEEE Trans. Wirel. Commun.*, vol. 20, no. 1, pp. 421-439, Jan. 2021.

[3] "6G The Next Hyper-Connected Experience for All." Samsung. Oct. 2021. [Online]. Available: https://research.samsung.com/nextgeneration communications.

[4] W. Stutzman and E. Coffey, "Radiation Pattern Synthesis of Planar Antennas Using The Iterative Sampling Method," in *IEEE Transactions on Antennas and Propagation*, vol. 23, no. 6, pp. 764-769, November 1975, doi: 10.1109/TAP.1975.1141173.

[5] Zhan Shi and Zhenghe Feng, "A New Array Pattern Synthesis Algorithm Using The Two-Step Least-Squares Method," in *IEEE Signal Processing Letters*, vol. 12, no. 3, pp. 250-253, March 2005, doi: 10.1109/LSP.2004.842282.

[6] H. Lebret and S. Boyd, "Antenna Array Pattern Synthesis Via Convex Optimization," in *IEEE Transactions on Signal Processing*, vol. 45, no. 3, pp. 526-532, March 1997, doi: 10.1109/78.558465.

[7] Y. Aslan, J. Puskely, A. Roederer and A. Yarovoy, "Phase-Only Control of Peak Sidelobe Level and Pattern Nulls Using Iterative Phase Perturbations," in *IEEE Antennas and Wireless Propagation Letters*, vol. 18, no. 10, pp. 2081-2085, Oct. 2019, doi: 10.1109/LAWP.2019.2937682.

[8] Khalaj-Amirhosseini M, "Phase-Only Synthesis of Planar Arrays Using Autocorrelation Matching Method," in *Int J RF Microw Comput Aided Eng.*, 2020; 30:e22153. https://doi.org/10.1002/mmce.22153

[9] W. Zhang, Y. Peng and Z. Zhang, "Efficient Phase-Only Symmetric Pattern Synthesis for Linear and Circular Planar Arrays via Phase Perturbation in Low-Dimensional Space," in *IEEE Transactions on Antennas and Propagation*, vol. 72, no. 2, pp. 1947-1952, Feb. 2024, doi: 10.1109/TAP.2023.3345413.

[10] Y. Shen, P. Leng, S. Chen and H. Li, "Phase-Only Transmit Beampattern Synthesis With Maximum Mainlobe Gain via Manifold ADMM," in *IEEE Antennas and Wireless Propagation Letters*, vol. 23, no. 1, pp. 184-188, Jan. 2024, doi: 10.1109/LAWP.2023.3321021.

[11] Khalaj-Amirhosseini M., "Synthesis of Linear and Planar Arrays with Sidelobes of Individually Arbitrary Levels", in *Int J RF Microw Comput Aided Eng.* 2019; 29:e21637. https://doi.org/10.1002/mmce.21637.

[12] P. Rocca, L. Poli, N. Anselmi and A. Massa, "Nested Optimization for the Synthesis of Asymmetric Shaped Beam Patterns in Subarrayed Linear Antenna Arrays," in *IEEE Transactions on Antennas and Propagation*, vol. 70, no. 5, pp. 3385-3397, May 2022, doi: 10.1109/TAP.2021.3137176.

[13] Z. Chen, Z. Song, H. Liu, J. Yu and X. Chen, "Passive-Shaped Beam Synthesis Using Pattern Diversity Dielectric Resonator Antenna Array," in *IEEE Antennas and Wireless Propagation Letters*, vol. 20, no. 7, pp. 1115-1119, July 2021, doi: 10.1109/LAWP.2021.3068995.

[14] J. Tian, S. Lei, Z. Lin, Y. Gao, H. Hu and B. Chen, "Robust Pencil Beam Pattern Synthesis With Array Position Uncertainty," in *IEEE Antennas and Wireless Propagation Letters*, vol. 20, no. 8, pp. 1483-1487, Aug. 2021, doi: 10.1109/LAWP.2021.3088095.

[15] Q. Wang, R. Gao and S. Liu, "Mapping-Based Optimization Method for Pattern Synthesis via Array Element Rotation," in *IEEE Transactions on Antennas and Propagation*, vol. 68, no. 4, pp. 2736-2742, April 2020, doi: 10.1109/TAP.2019.2951546.

[16] S. E. Nai, W. Ser, Z. L. Yu and H. Chen, "Beampattern Synthesis for Linear and Planar Arrays With Antenna Selection by Convex Optimization," in *IEEE Transactions on Antennas and Propagation*, vol. 58, no. 12, pp. 3923-3930, Dec. 2010, doi: 10.1109/TAP.2010.2078446.

[17] X. Cai and H. V. Cheng, "Array Pattern Synthesis with Discrete Phases for Reconfigurable Intelligent Surfaces," in Proc. *2024 IEEE 25th International Workshop on Signal Processing Advances in Wireless Communications (SPAWC)*, Lucca, Italy, 2024, pp. 741-745, doi: 10.1109/SPAWC60668.2024.10694155.

[18] Longyao Ran, Shengyao Chen, Feng Xi, "Beampattern Synthesis for Active RIS-Assisted Radar with Sidelobe Level Minimization," in *Signal Processing*, Volume 206, 2023, 108925, ISSN 0165-1684, https://doi.org/10.1016/j.sigpro.2022.108925.

[19] Xiong, R., Lu, J., Yin, K., Mi, T., & Qiu, R. C. (2024), "Fair Beam Synthesis and Suppression via Transmissive Reconfigurable Intelligent Surfaces." in ArXiv. [Available online] https://arxiv.org/abs/2411.02008.

[20] T. E. Rimpiläinen and R. Jäntti, "Multiple Scattering Model for Beam Synthesis With Reconfigurable Intelligent Surfaces," in *IEEE Transactions on Antennas and Propagation*, vol. 71, no. 6, pp. 4990-5000, June 2023, doi: 10.1109/TAP.2023.3262638.

[21] Rahal, M., Denis, B., Keykhosravi, K. et al. "Performance of RIS-Aided Near-Field Localization Under Beams Approximation from Real Hardware

Characterization." in *J Wireless Com Network 2023*, 86 (2023). https://doi.org/10.1186/s13638-023-02294-9.

[22] H. S. Yoon, D. G. Jo, D. I. Kim and K. W. Choi, "On-Off Arbitrary Beam Synthesis and Non-Interactive Beam Management for Phased Antenna Array Communications," in *IEEE Transactions on Vehicular Technology*, vol. 70, no. 6, pp. 5959-5973, June 2021, doi: 10.1109/TVT.2021.3078781.